

Radiation-dose effects in correlative X-ray/cryo-electron microscopy of frozen-hydrated biological samples

Thorsten B. Blum,^{a,*} Vincent Olieric,^b Ana Diaz,^b Takashi Ishikawa^{a,c} and Volodymyr M. Korkhov^{a,d,*}

Received 10 October 2025

Accepted 11 February 2026

Edited by E. F. Garman, University of Oxford, United Kingdom

This article is part of the Proceedings of the 12th International Workshop on X-ray Radiation Damage to Biological Crystalline Samples.

Keywords: cryo-X-ray tomography; cryo-electron microscopy; correlative microscopy.

EMDB references: apoferritin, 0 MGy, EMD-55343; 1 MGy, EMD-55338; 100 MGy, EMD-55344

Supporting information: this article has supporting information at journals.iucr.org/d

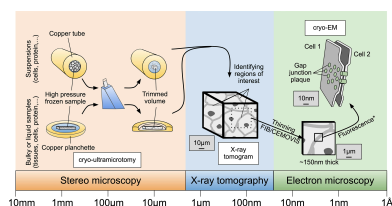
^aPSI Center for Life Sciences, Paul Scherrer Institute, 5232 Villigen PSI, Switzerland, ^bPSI Center for Photon Science, Paul Scherrer Institute, 5232 Villigen PSI, Switzerland, ^cDepartment of Biology, ETH Zürich, 8093 Zürich, Switzerland, and ^dInstitute of Molecular Biology and Biophysics, ETH Zürich, 8093 Zürich, Switzerland. *Correspondence e-mail: thorsten.blum@psi.ch, volodymyr.korkhov@psi.ch

In cryo-electron microscopy (cryo-EM), imaging of biological specimens is restricted by the limited field of view and by sample thickness. Hard X-ray imaging, with its ability to penetrate samples several tens of micrometres thick, offers a complementary approach for high-resolution visualization. A major concern is whether cryo-preserved samples can withstand the handling conditions at synchrotron facilities without excessive icing, and whether the radiation exposure during X-ray imaging compromises specimen integrity, thereby hindering subsequent attempts to achieve high-resolution 3D reconstructions via cryo-EM. To evaluate this, we deposited apoferritin samples on a cryo-EM grid, exposed them to varied X-ray doses typical for X-ray tomography experiments at a synchrotron facility, and subsequently analysed the exposed particles by cryo-EM. Despite the apparent damage sustained throughout the experiment, the samples remained amenable to cryo-EM analysis, with structural details at a resolution of ~ 4 Å at the highest absorbed X-ray dose of 100 MGy. By comparison, a similar cryo-EM dataset of apoferritin particles that were not exposed to X-rays but were mounted on the same cryo-EM grid resulted in a 3D reconstruction at 3.17 Å resolution. Thus, while radiation damage may limit the high-resolution information in specimens processed by cryo-X-ray tomography, the cryo-preserved biological material exposed to these high X-ray doses can still be used for subsequent cryo-EM workflows aiming to obtain structural biology insights at intermediate to high resolution. These findings lay the groundwork for an integrated imaging workflow that combines X-ray and cryo-EM techniques to enable multiscale analysis of thick vitrified biological specimens.

1. Introduction

Cryo-electron microscopy (cryo-EM) is a foundational technique in structural biology renowned for its ability to produce high-resolution data of biological specimens (Kühlbrandt, 2014; Saibil, 2022). It allows researchers to visualize intricate cellular architectures and protein complexes, thereby deepening our insight into complex biological mechanisms. However, achieving multiscale high-resolution imaging with cryo-EM remains challenging due to constraints such as a limited field of view and the necessity for very thin samples amenable to transmission EM analysis.

Given the limited field of view of cryo-EM, employing multiscale imaging techniques before cryo-EM is essential for effective sample characterization and for targeting the regions of interest. This process remains challenging, not only because of the restricted imaging area but also due to the need for thin, electron-transparent frozen-hydrated specimens. To overcome



these hurdles, correlative light and electron microscopy (CLEM) has proven to be a valuable approach for pinpointing regions of interest within frozen biological samples, whether at room temperature (Shafiei *et al.*, 2025) or under cryogenic conditions (Klein *et al.*, 2021).

However, despite their utility, CLEM approaches rely on fluorescence of the objects of the target structures to identify the region of interest when employing the waffle method, in which the sample is vitrified on an EM grid through high-pressure freezing (Kelley *et al.*, 2022; Klykov *et al.*, 2022). X-ray imaging presents a compelling alternative, offering the capacity to image thick, unstained samples across a broader field of view. The integration of hard X-ray nano-tomography (Shahmoradian *et al.*, 2017; Longo *et al.*, 2020; Kuan *et al.*, 2020) with cryo-EM may facilitate the visualization of large and complex biological specimens with volumes up to $100 \times 100 \times 100 \mu\text{m}$, while also allowing the precise targeting of specific regions for detailed analysis using cryo-electron tomography (cryo-ET).

To integrate the various techniques, we aim to develop a workflow of processes to achieve this in the long term (Fig. 1). For this purpose, the biological samples must first undergo cryo-fixation under cryogenic conditions, which can consist of plunge-freezing in liquid ethane, as is performed for samples thinner than about $10 \mu\text{m}$ and which can be imaged by cryo soft X-ray tomography (Groen *et al.*, 2019, 2025; Guo &

Larabell, 2019). However, for samples thicker than about $10 \mu\text{m}$, the sample preparation may require high-pressure freezing followed by trimming with an ultramicrotome (Fig. 1a; Holler *et al.*, 2017). Hard X-ray nano-tomography can then be employed to locate regions of interest (Fig. 1b), which may be thinned using focused ion-beam (FIB; Marko *et al.*, 2006; Rigort *et al.*, 2012) milling or cryo-electron microscopy of vitreous sections (CEMOVIS; Studer *et al.*, 2001; Al-Amoudi *et al.*, 2004). Finally, these thinned areas can be imaged using cryo-EM, aiming to obtain 3D reconstructions with high (subnanometre) spatial resolution (Fig. 1c). Fig. 1 shows the envisioned workflow for correlative hard X-ray nano-tomography of tissues and cryo-EM.

To the best of our knowledge, correlative imaging combining cryo hard X-ray nano-tomography and cryo-ET has not been successfully performed to date. Only individual steps of the entire pipeline (Fig. 1) under room-temperature or cryo conditions have been demonstrated to confirm their feasibility. For example, it has been shown that cryo-preserved samples can be prepared and successfully analysed by X-ray nano-tomography (Holler *et al.*, 2017). Although the tomograms of frozen samples were not correlated for region-of-interest (ROI) extraction, studies involving fixed biological samples have demonstrated that ROIs identified through micro-computed tomography (micro-CT) can be trimmed with a microtome and subsequently transferred to a focused ion-

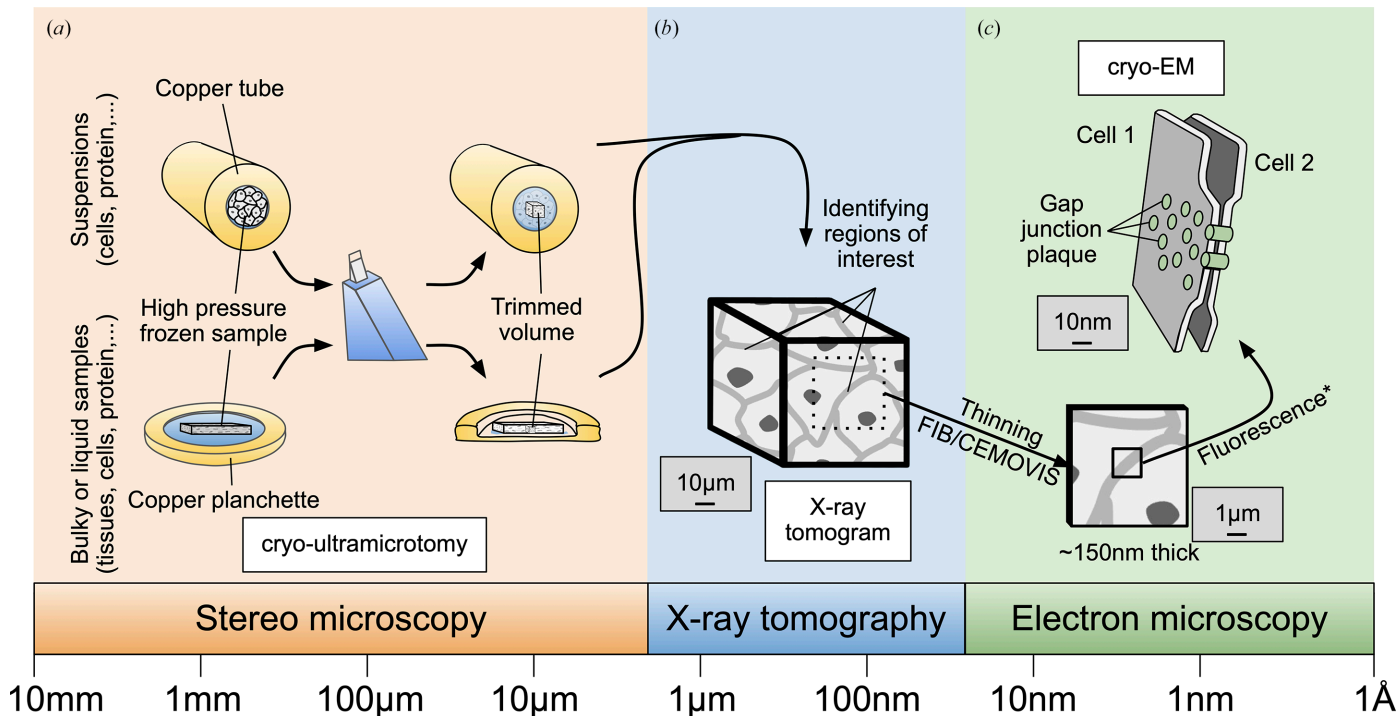


Figure 1 Schematic workflow of the process envisioned for correlative hard X-ray nano-tomography and cryo-EM. The purpose of this workflow is to identify a region of interest (for example a gap-junction plaque at the cell–cell interface, illustrated here). To achieve this, (a) cells are subjected to high-pressure freezing within copper tubes (inner diameter $350 \mu\text{m}$) or tissues are embedded in copper planchettes with a $200 \mu\text{m}$ cavity. These samples are then precisely trimmed using a diamond knife to yield a rectangular section measuring approximately $70 \times 70 \mu\text{m}$ in area and $30 \mu\text{m}$ in thickness, optimized for hard X-ray nano-tomography. (b) An X-ray tomogram of the trimmed volume is acquired, allowing the identification of regions of interest (ROIs). (c) Thin sample layers are then extracted from selected ROIs using either cryo-electron microscopy of vitreous sections (CEMOVIS) or focused ion-beam (FIB) milling (*optionally guided by fluorescence light microscopy if fluorescence markers are present) for downstream cryo-EM analysis.

beam scanning electron microscope for imaging in scanning electron microscopy (SEM) mode (Karreman *et al.*, 2016).

Other studies have demonstrated that cryo-light/fluorescence can be correlated with cryo soft X-ray tomography (Okolo *et al.*, 2021). Likewise, light/fluorescence correlated with hard X-ray tomography (correlative single-cell hard X-ray computed tomography and X-ray fluorescence imaging) or correlating soft X-ray tomography under non-cryo conditions with nonbiological specimens using scanning transmission electron microscopy (STEM) has been demonstrated (Lo *et al.*, 2019). While these developments mark significant progress, they do not address key questions surrounding the integration of cryo-X-ray nano-tomography with cryo-ET. Crucially, uncertainties remain about (i) whether cryo-preserved samples can endure the handling at the synchrotron facilities without becoming excessively icy and (ii) whether the radiation doses absorbed during X-ray imaging compromise the integrity of the specimen, limiting any subsequent efforts aimed at obtaining high-resolution 3D reconstructions by cryo-EM.

X-ray damage is classified into primary and secondary damage (Henderson, 1995; Nass, 2019). Primary damage results from the direct interaction between the radiation beam and electrons, resulting in the ejection of energetic electrons from atoms through processes such as the photoelectric effect, Auger effect and Compton scattering. These events can break chemical bonds, causing molecular degradation. Secondary damage arises from the reactions of radiolytic products, such as free radicals generated by these energetic electrons. This radiation-induced damage results in the degradation of image resolution during subsequent EM processing.

Radiation damage has previously been extensively investigated using X-ray crystallography of crystalline samples (Garman & Weik, 2023). Early insights were provided by Henderson (1990), who predicted that exposure to X-ray doses of approximately 20 MGy at nitrogen temperatures would destroy half of the intensity of crystalline diffraction patterns in protein crystals, supported experimentally by Gonzalez & Nave (1994). Furthermore, Teng & Moffat (2000) demonstrated through diffraction experiments that lysozyme crystals could withstand up to 16 MGy and still achieve a resolution of 1.6 Å (Teng & Moffat, 2000). Additionally, Owen and coworkers reported that apoferritin crystals exhibited significant intensity loss, of 50% or more, when subjected to 43 MGy for a resolution range of 2.6–2.5 Å or 200 MGy for lower resolution ranges of 20–10 Å (Owen *et al.*, 2006). In single proteins, high-resolution structural information is particularly susceptible to damage, as radical formation from X-ray exposure often compromises sensitive side chains (Teng & Moffat, 2000; Owen *et al.*, 2006). How the X-ray dose affects amorphous frozen samples that more closely resemble typical biological samples (cells, tissues *etc.*) has not been evaluated so far, to the best of our knowledge.

Here, we tested whether exposure of biological samples to radiation doses typically used in hard X-ray nano-tomography (Shahmoradian *et al.*, 2017) would still preserve the structural information at high resolution, a prerequisite for developing a

cryo-correlative workflow for combining X-ray imaging with cryo-EM. Typical doses reported in the literature for frozen-hydrated tissues are between 1 and 20 MGy (Shahmoradian *et al.*, 2017; Holler *et al.*, 2017); however, we expect that doses up to 100 MGy could be absorbed, for example by ptychographic X-ray computed tomography at fourth-generation synchrotron sources. An exposure of 100 MGy required for recording a ptychographic X-ray computed tomogram corresponds to a pre-exposure of approximately $27 \text{ e}^- \text{ \AA}^{-2}$ when using a 300 keV electron microscope with a conversion factor of 3.7 (Dickerson *et al.*, 2024; Groen *et al.*, 2025). Cryo-EM studies have demonstrated that datasets exposed to ~ 19 or $\sim 24 \text{ e}^- \text{ \AA}^{-2}$ at 300 keV, after discarding the initial movie frames, still yielded reconstructions at 3.35 Å resolution (Grant & Grigorieff, 2015) and 3.94 Å resolution (Allegretti *et al.*, 2014), using particle alignments derived from the full, dose-weighted movies. Experiments assessing pre-exposure with X-rays or electrons suggest that following the acquisition of a ptychographic X-ray computed tomogram, the resolution should remain sufficient to trace the protein backbone.

However, in cryo-correlative workflows that combine X-ray imaging with cryo-EM, it is essential to consider the cumulative radiation dose absorbed by biological specimens during both modalities. To assess the radiation effects, we chose an *in vitro* sample, apoferritin, as a particularly suitable specimen that can be frozen on cryo-EM grids in thin ice, yields high-resolution density maps in cryo-EM analysis and should thus enable precise assessment of the combined effects of X-rays and electrons on biological structures.

2. Methods

2.1. Apoferritin on EM grids

Purified apoferritin (30 µl) derived from equine spleen (Sigma–Aldrich) was desalted using a Micro Bio-Spin column (Bio-Rad) into a Tris buffer (20 mM Tris–HCl pH 7.5, 300 mM NaCl). Aliquots of 3 µl apoferritin at a concentration of $\sim 0.85 \text{ mg ml}^{-1}$ were applied onto glow-discharged Quantifoil Cu200 R1.2/1.3 holey carbon EM grids or Quantifoil Au200 R2/2 holey carbon EM finder grids. Grids were blotted for 2 s with a blot force of 10 and plunge-frozen in liquid ethane using a Vitrobot (Thermo Fisher Scientific) with the environmental chamber set to 100% humidity and 8°C. Grids prepared in this way were stored in liquid nitrogen before imaging.

2.2. X-ray radiation exposure

EM grids were mounted in AutoGrid rings and secured with C-clips (Thermo Fisher Scientific). These clipped grids were then placed into holders compatible with SPINE vials (Huang *et al.*, 2020) and shipped to the European Synchrotron Radiation Facility (ESRF) in Grenoble, France. Using a vacuum cryo-transfer system in liquid nitrogen (LN₂), the sample holders were transferred to the loading carrier. Exposures were conducted at 100 K at the ID30B beamline of the ESRF using a photon energy of 13.5 keV, a beam size of $30 \times 30 \text{ µm}$ and a flux of $1.0 \times 10^{13} \text{ photons s}^{-1}$. Areas of $90 \times$

Table 1
Cryo-EM structure determination.

	0 MGy	1 MGy	100 MGy
Data collection			
Magnification	76923×	76923×	76923×
Pixel size (Å)	0.65	0.65	0.65
Defocus range (µm)	−0.6 to −2.4	−0.6 to −2.4	−0.6 to −2.4
Voltage (kV)	300	300	300
Exposure time (s)	0.92	0.92	0.92
Total dose (e Å ^{−2})	60	60	60
No. of frames (TIF)	40	40	40
Dose per frame (e Å ^{−2})	1.5	1.5	1.5
No. of movies	760	405	565
Reconstitution			
Automatically picked particles	60105	48194	80664
After 2D classification (particles)	33386	8548	13728
After 3D classification (particles)	30265	6488	9547
Final overall resolution (Å)	2.83	3.51	3.71
Estimated map-sharpening <i>B</i> factor (Å ²)	−80	−99	−100
Randomly equally picked particles	6488	6488	6488
EMDB accession No.	EMD-55343	EMD-55338	EMD-55344
Final overall resolution (Å)	3.17	3.56	3.88
Estimated map-sharpening <i>B</i> factor (Å ²)	−63	−83	−97

90 µm field of view were exposed using the mesh-scan function of *MXCuBE* (Bowler *et al.*, 2010). The beam follows a continuous snake-like trajectory, resulting in estimated radiation doses of 1 and 100 MGy, while the maximum variation in the exposed volume was around 9%. The radiation dose was calculated using equation (5) from *A beginner's guide to radiation damage* (Holton, 2009), without accounting for the sample thickness, and applying exposure times of 0.213 and 21.3 s.

2.3. Cryo-TEM imaging

Data were acquired on a Titan Krios G3i electron microscope at 300 keV (Thermo Fisher Scientific), with a GIF BioQuantum filter (20 eV slit width) and a K3 Summit electron-counting direct detection camera (Gatan) at a magnification of 76 923×, resulting in a pixel size of 0.65 Å, using *EPU* (Thermo Fisher Scientific). The defocus varied between −0.6 and −2.4 µm. Overall, 1730 movies were recorded with a total dose of 60 e[−] Å^{−2} per movie (0.92 s exposure in total, 40 frames in total). Of these, for 0, 1 and 100 MGy, the number of movies was 760, 405 and 565, respectively (Table 1).

2.4. Image processing/data analysis

For image processing, the single-particle cryo-EM analysis software package *RELION5* (Scheres, 2012) was used. The movies were drift-corrected and dose-weighted using *RELION*'s own implementation of the *MotionCor2* algorithm (Zheng *et al.*, 2017), and the contrast transfer function parameters were estimated from the motion-corrected electron micrographs using *CTFFIND4* (Rohou & Grigorieff, 2015). Apoferritin particles were automatically picked by using three 2D classes of apoferritin. Boxes with a size of 512 pixels, rescaled to 64 pixels, were extracted. Several rounds of 2D classification and one 3D classification were performed. For the first 3D classification a map obtained from *EMPIAR-*

11273 was used as the initial reference. The reference was low-pass filtered to 60 Å and an octahedral symmetry was applied for all 3D runs. Only good classes were extracted with boxes of 400 pixels, without re-scaling. An additional round of 3D classification was performed, followed by 3D refinement and post-processing using automatic *B*-factor estimation. For post-processing, a mask was generated in *RELION5* from the refinement maps by extending the binary maps by ten pixels and adding a soft edge by 20 pixels. Subsequently, Bayesian polishing and CTF refinement were carried out to estimate (i) higher order aberrations, including beam tilt, trefoil and fourth-order aberrations, (ii) anisotropic magnification and (iii) per-particle defocus by CTF parameter fitting, including defocus fitting per particle and astigmatism fitting per micrograph. For the final refinement, the number of randomly selected particles used for each dataset was equalized to 6488 particles for a fair comparison. The Rosenthal–Henderson *B* factors were calculated as a quality metric using the *bfactor_plot.py* script (Zivanov *et al.*, 2018) in *RELION5* (Table 2).

3. Results

3.1. Exposing apoferritin on EM grids to X-rays

Desalted apoferritin samples were applied to different grid types (see Section 2), plunge-frozen and secured in AutoGrid rings to enhance stability. These AutoGrid rings were transferred on specialized 3D-printed holders for X-ray radiation exposure (Huang *et al.*, 2020), stored under liquid nitrogen and transported to beamline ID30B at the ESRF. Regions of the grids were exposed to X-ray radiation at a photon energy of 13.5 keV, absorbing doses of 1 and 100 MGy (see Section 2 for details of the dose calculation), which are within the range commonly used for X-ray nano-tomography. Following exposure, the samples were recovered under cryogenic

Table 2
Rosenthal–Henderson B factors.

Res, resolution.

N	$\ln(N)$	0 MGy		1 MGy		100 MGy	
		Res (Å)	$1/\text{Res}^2$ (Å ⁻²)	Res (Å)	$1/\text{Res}^2$ (Å ⁻²)	Res (Å)	$1/\text{Res}^2$ (Å ⁻²)
100	4.605	13.68	0.0053	13.68	0.0053	13.68	0.0053
200	5.298	8.12	0.0151	8.97	0.0124	13.68	0.0053
400	5.991	8.12	0.0151	4.48	0.0498	8.12	0.0151
800	6.685	4.00	0.0625	4.13	0.0587	6.05	0.0274
1600	7.378	3.82	0.0684	4.00	0.0625	4.41	0.0515
3200	8.071	3.42	0.0854	3.61	0.0767	4.13	0.0587
6400	8.764	3.25	0.0947	3.51	0.0810	3.88	0.0664
6488	8.778	3.17	0.0995	3.56	0.0788	3.88	0.0664
Estimated B factor (Å ²)		83.99		111.90		120.18	
Estimated Res with 9732 particles (Å)		3.03		3.28		3.67	
Estimated Res with 12976 particles (Å)		2.94		3.19		3.56	
Estimated Res with 25952 particles (Å)		2.75		3.01		3.32	
Estimated Res with 51904 particles (Å)		2.59		2.85		3.13	

temperature, shipped to the ScopeM facility at ETH Zurich and analysed by cryo-EM and single-particle analysis. Several issues arose during the experiment, including ice contamination, damage to the support film, damage to the grid bars (Fig. 2) and, in some cases, the grids detaching from the holders. Of the two grid types tested, the more fragile Quantifoil Au200 R2/2 holey carbon EM finder grids did not survive handling, whereas the Quantifoil Cu200 R1.2/1.3 holey carbon EM grids withstood the mechanical stress. The specialized 3D-printed holders are not well suited for handling frozen cryo-EM grids (Fig. 3a) under liquid nitrogen, as the plastic arms become rigid and brittle at cryogenic temperatures (Fig. 3a). This creates difficulties when inserting the grid for two main reasons. Firstly, if the holders are too tight, the grid cannot be inserted at all, requiring the holder to be warmed up before another attempt can be made. Secondly, if the holders are not sufficiently tight prior to cooling, the grid is inadequately secured and may fall out during handling, which could explain why, in some cases, grids became detached during shipment. Nevertheless, despite these challenges, one of the grids that had been exposed to 0, 1 and 100 MGy in different grid squares was still suitable for cryo-EM data collection.

3.2. Analysing apoferritin on exposed EM grids using cryo-TEM

Figs. 3(c) and 3(d) show an atlas of the grid acquired by cryo-EM, which was correlated with the image recorded at the X-ray crystallography beamline to locate the exposed areas. The processed grids displayed a high degree of ice contamination in comparison to the freshly prepared EM grids, but the grid remained in good condition relative to the other grids sent to the synchrotron (Fig. 2). The relatively unbroken areas devoid of large ice clumps were selected for the final data acquisition. Even in the best regions of the grids, the micrographs displayed noticeable ice contamination (Supplementary Fig. S1a). Particles were automatically picked using a template and then subjected to multiple rounds of 2D and 3D classification to eliminate incorrectly picked, contaminated or poor-

quality particles (Supplementary Figs. S1a and S1b). This iterative cleaning ensured that only well defined apoferritin particles were retained for further analysis. The selected particles were subsequently refined through CTF correction and polishing to improve data quality. To enable a fair comparison across conditions, the number of particles was normalized to 6488 for each of the three data sets before final 3D refinement and post-processing. The resulting reconstructions demonstrated that although higher radiation doses increasingly affected the samples, the high-resolution structural information was preserved in all cases, with each test dataset yielding a robust reconstruction (Fig. 4, Table 1).

As expected, the particle selections from regions that had not been exposed to X-rays reached the highest resolution of 3.17 Å. Remarkably, the cryo-EM reconstructions of apoferritin that absorbed X-ray doses of 1 and 100 MGy reached resolutions of 3.56 and 3.88 Å, respectively (Fig. 4b). In line with this trend, the Rosenthal–Henderson B factors also indicate diminished particle quality in the irradiated regions, rising from 83.99 Å² at 0 MGy to 111.90 Å² at 1 MGy and 120.18 Å² at 100 MGy (Table 2). The level of detail preserved in the cryo-EM maps at this resolution would effectively allow macromolecular model building at near-atomic resolution, demonstrated in Fig. 4(c) by the density quality that permits reliable fitting of the model (PDB entry 6rjh; Naydenova *et al.*, 2019). To ensure that the higher resolution was not simply an effect of ice thickness, micrographs were checked by eye and analysed with *CTFFIND4* (Rohou & Grigorieff, 2015) for ice-ring density (Supplementary Fig. S2). Both methods revealed more ice crystals in areas that had been exposed to X-rays. The pronounced increase in ice-related features in the exposed region, likely arising from both surface accumulation and local heating of the sample towards the devitrification temperature, probably accounts for the large number of particles excluded during 2D classification in the exposed area (82.3% and 83.0%) compared with the non-X-ray-exposed area (44.4%).

To check whether the resolution decrease was due to ice buildup, a dataset collected from a sample that had not been

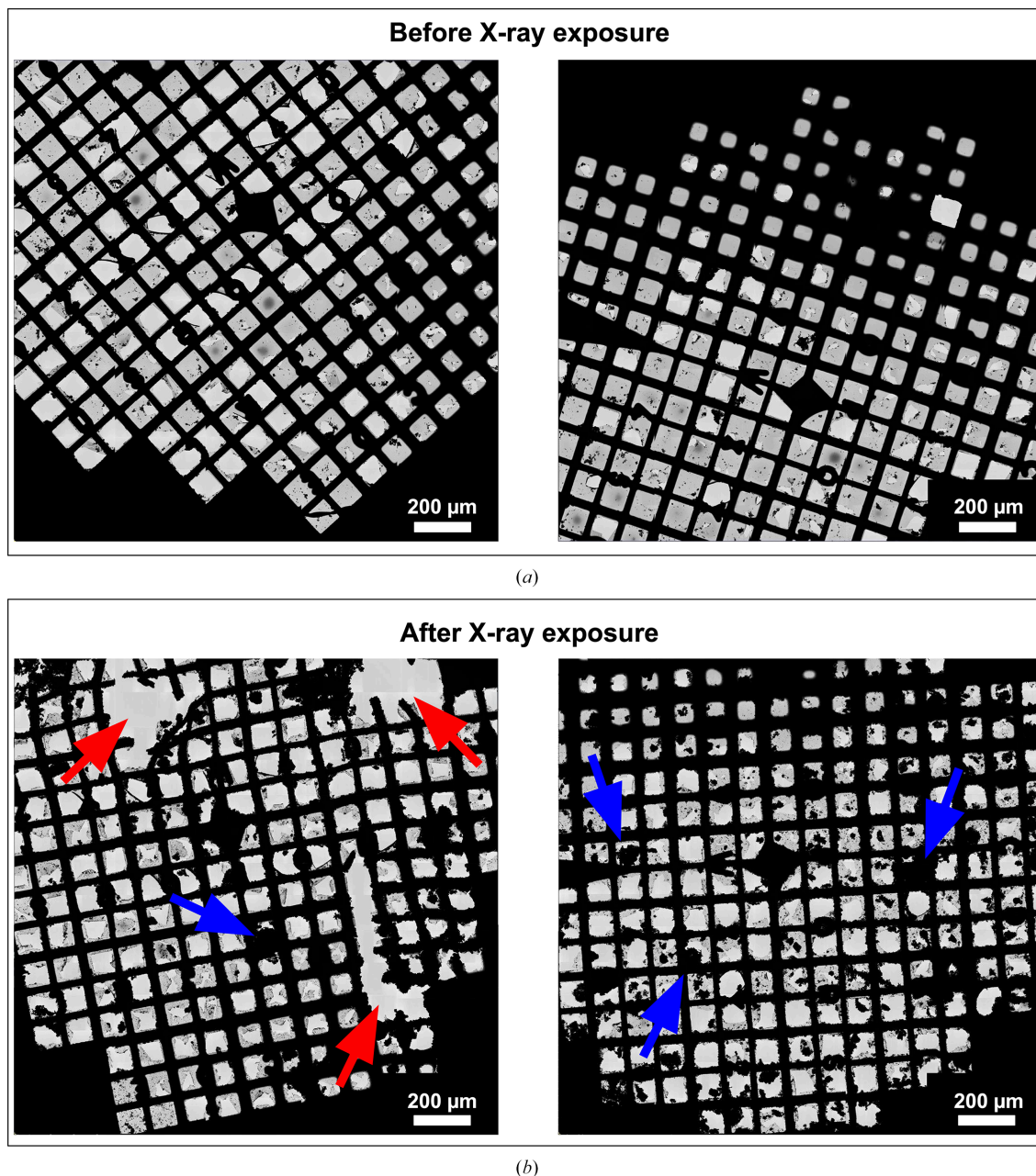


Figure 2

Cryo-TEM images of grids before and after X-ray irradiation. (a, b) Representations of two grids before (a) and after (b) shipment to the synchrotron, exposure to X-rays and shipment back in a dry shipper. The equivalent positions on the grids with either mechanical damage or ice contamination are indicated by red and blue arrows, respectively.

exposed to X-rays was processed without the first frame, corresponding to a pre-exposure of $1.5 \text{ e}^- \text{ \AA}^{-2}$ ($\sim 5.55 \text{ MGy}$ using a conversion factor of 3.7; Dickerson *et al.*, 2024; Groen *et al.*, 2025). The dataset only showed a slight increase in ice and a resolution drop of 0.25 \AA to 3.42 \AA (Supplementary Fig. S3). Taken together, these findings indicate that resolution changes result from the combined effects of ice accumulation and radiation damage. Importantly, they also demonstrate that even a combination of the highest absorbed X-ray dose of 100 MGy with a typical cryo-EM data-collection workflow (accumulating a total dose of $60 \text{ e}^- \text{ \AA}^{-2}$ per movie stack) preserves the protein structure in this experimental format, *i.e.*

purified protein in a thin film of vitreous ice, sufficiently for most structural biology applications at high resolution.

4. Discussion

Multiscale correlative imaging of biological samples using X-rays and electrons has tremendous potential in light of the recent breakthroughs in both of these techniques (Shafiei *et al.*, 2025; Klein *et al.*, 2021; Okolo *et al.*, 2021; Lo *et al.*, 2019). However, as both approaches are known to cause severe radiation damage to the objects of interest during imaging, a major question has been whether combining X-ray and

cryo-EM analysis of intact frozen-hydrated biological samples might destroy the atomic structures within the sample of interest, thereby rendering any meaningful high-resolution analysis largely impossible. Our results show that the absorption of a combination of a typical X-ray tomography radiation dose and a typical cryo-EM imaging dose preserves the high-resolution information in the sample, sufficient to reach near-atomic 3D reconstructions for a model biological sample. When 100 MGy is converted to $e^- \text{Å}^{-2}$ at 300 keV using the factor of 3.7 (Dickerson *et al.*, 2024; Groen *et al.*, 2025), our findings are consistent with cryo-EM studies reporting that exposures of ~ 19 and $\sim 24 e^- \text{Å}^{-2}$ at 300 keV yielded reconstructions of 3.35 Å (Grant & Grigorieff, 2015) and 3.94 Å (Allegretti *et al.*, 2014), respectively, achieved with X-rays rather than electrons.

These results provide a strong foundation for developing a correlative imaging workflow combining cryo hard X-ray tomography and cryo-EM. Such a pipeline would allow multiscale imaging of thick biological specimens in a near-native frozen-hydrated state. In addition to validating this correlative imaging technique, our results, on one hand, reinforce the previous findings from X-ray crystallography regarding radiation-induced damage to protein crystal structures (Henderson, 1990; Gonzalez & Nave, 1994; Teng & Moffat, 2000; Owen *et al.*, 2006) and, on the other hand, provide a new perspective on studying X-ray radiation damage in the absence of a crystalline lattice as the major component. Remarkably, we show that a sample subjected to an intense X-ray dose of 100 MGy still yields a resolution of

3.88 Å when imaged via cryo-EM. This finding is highly significant as it suggests that structural integrity can be preserved even under harsh experimental conditions, broadening the range of feasible sample treatments in hybrid workflows.

The type of sample plays a key role: in this study, we demonstrated that thin samples used directly for cryo-EM lose resolution from both radiation damage and ice accumulation during X-ray exposure. By contrast, in workflows that combine hard X-ray nano-tomography with cryo-EM, thick samples are imaged at the synchrotron and then thinned to isolate regions of interest. Thinning removes the ice contamination introduced by X-rays, making these hybrid approaches especially effective.

However, there are limitations to our ability to interpret the results obtained with the thin model system here (*i.e.* apoferritin molecules suspended in a thin film of vitreous ice). It is conceivable that the exposure of a much thicker frozen biological sample, such as a tissue biopsy, will result in the generation of more radicals due to X-ray interaction with the bulky specimen, leading to substantially more radiation damage than we have observed here. Careful experimentation will be needed to determine whether there are fundamental differences in the damage suffered by the thin and thick amorphous biological specimens.

Throughout the course of this research, we encountered two practical challenges while switching between X-ray microscopy and cryo-EM that warranted attention: (i) mechanical damage to the EM grid resulting from improper handling or

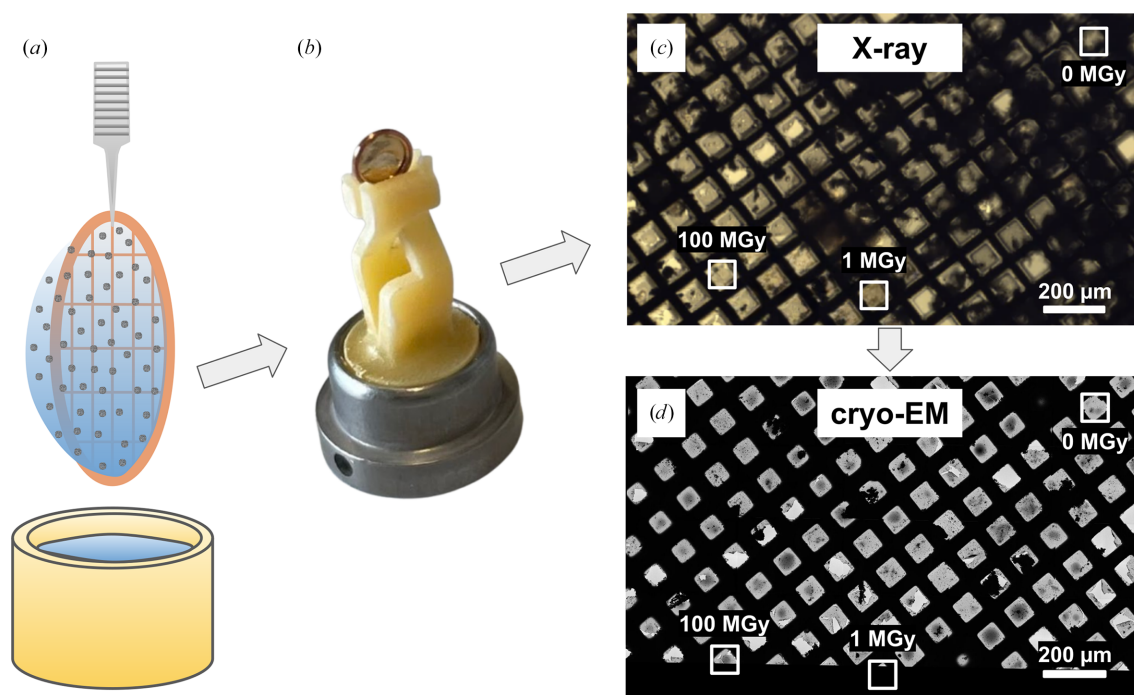
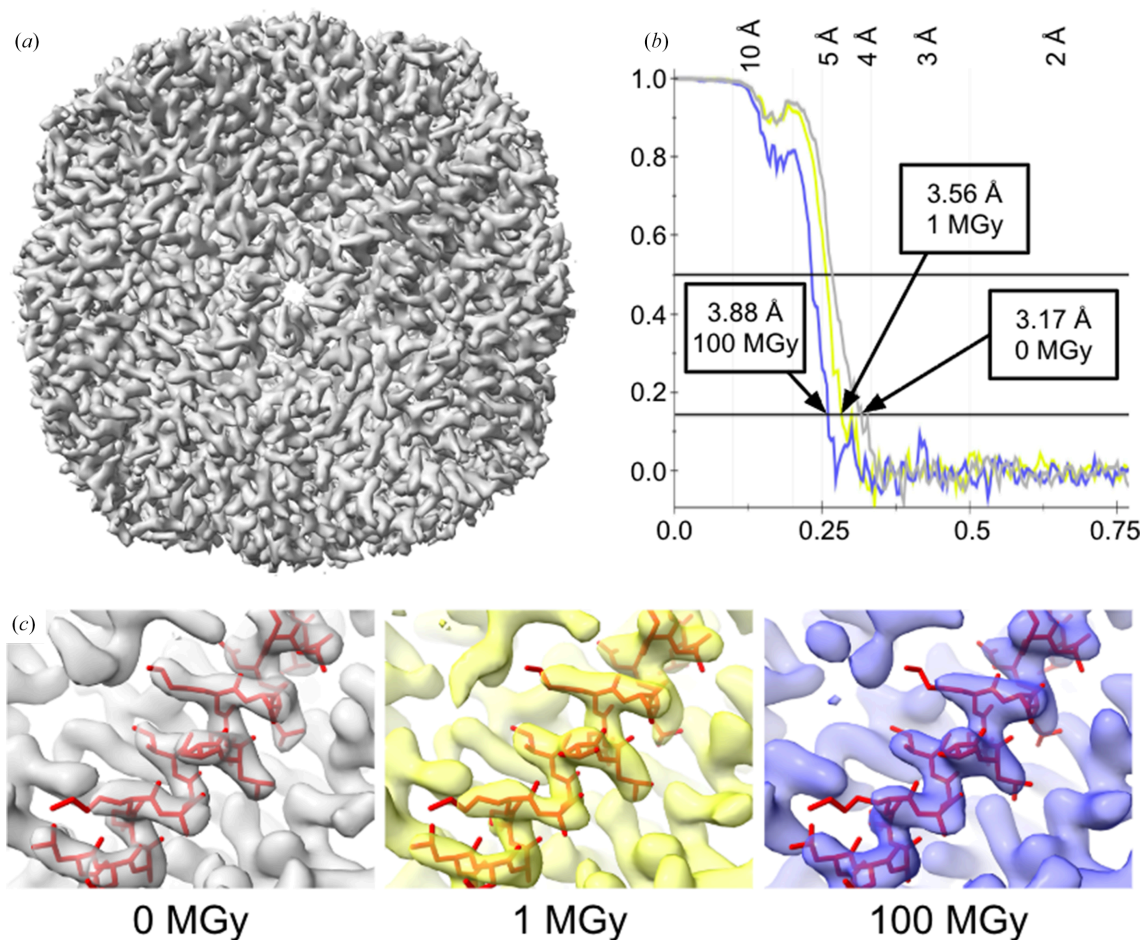


Figure 3

Correlation of synchrotron and cryo-EM imaging of frozen-hydrated apoferritin. (a) Apoferritin was plunge-frozen in liquid ethane. (b) The grid was clipped into AutoGrid rings and mounted onto custom 3D-printed holders. (c) At the beamline, the sample was transferred into the loading carrier, optically monitored with a camera and exposed to varying absorbed X-ray doses across selected grid squares. (d) The same grid squares were subsequently imaged by cryo-TEM and data were recorded.


Figure 4

Apoferritin single-particle data analysis and final resolution estimation. (a) Complete electron-density map of apoferritin from 6488 particles without X-ray exposure. (b) The Fourier shell correlation analysis of the three maps yielded resolutions of 3.17 Å for the dataset without X-ray exposure and 3.56 and 3.88 Å for the apoferritin samples which had absorbed 1 and 100 MGy X-ray doses, respectively. All three reconstructions were based on the same number of particles. These results indicate that higher X-ray exposure doses caused progressive protein damage, leading to a loss of resolution. (c) The apoferritin model (PDB entry 6rjh; Naydenova *et al.*, 2019) was fitted into all three maps to illustrate that each electron-density map distinctly reveals the backbone and side-chain densities, even though the side-chain densities in the 100 MGy map appear noticeably weaker.

exposure procedures, including incorrect grid orientation and autoloader miscalibration or misalignment, and (ii) the presence of ice contamination arising during sample transfer. While these issues impacted the initial tests, they are unlikely to persist in the finalized protocol. To mitigate these risks, the refined workflow will use a larger biological sample embedded in a high-pressure frozen block mounted on a copper tube. This setup offers increased mechanical stability during the imaging and transfer procedures. Following X-ray analysis, thin lamellae or cryo-sections will be prepared from the internal regions of the block, areas shielded from direct exposure in the X-ray microscope, thereby greatly reducing the risk of ice contamination and preserving sample quality for EM imaging. We anticipate that additional challenges will emerge, such as effective identification of the ROIs for lamella preparation via FIB or sectioning via CEMOVIS.

Together, these findings present a compelling case for a robust, integrated workflow bridging cryo hard X-ray microscopy and cryo-EM without compromising high-resolution data from biological samples. The demonstrated compatibility

of the two modalities, along with practical solutions for minimizing damage and contamination, as well as a great potential for integrating additional imaging modalities, such as light microscopy, to facilitate targeting of the regions of interest for high-resolution cryo-EM imaging, positions this approach as a powerful tool for enhancing imaging workflows and future structural biology investigations. By leveraging X-ray tomography to map the frozen intact tissues and to identify biologically relevant regions, researchers may be able to apply cryo-ET or single-particle analysis with near-atomic precision, thus expanding the capabilities of electron microscopy in studying complex biological systems.

Acknowledgements

We acknowledge the support and assistance of the staff at beamline ID30B at ESRF, with particular thanks to Andrew McCarthy, and at the ScopeM facility at ETH Zurich, with special thanks to Miroslav Peterek and Bilal Qureshi. We also

thank Spencer Bliven and Greta Assmann (PSI) for their support with high-performance computing.

Conflict of interest

The authors declare no competing interests.

Data availability

The datasets have been deposited in the Electron Microscopy Data Bank (EMDB) under accession numbers EMD-55343 (0 MGy), EMD-55338 (1 MGy) and EMD-55344 (100 MGy).

References

- Al-Amoudi, A., Chang, J.-J., Leforestier, A., McDowall, A., Salamin, L. M., Norlén, L. P. O., Richter, K., Blanc, N. S., Studer, D. & Dubochet, J. (2004). *EMBO J.* **23**, 3583–3588.
- Allegretti, M., Mills, D. J., McMullan, G., Kühlbrandt, W. & Vonck, J. (2014). *eLife*, **3**, e01963.
- Bowler, M. W., Guijarro, M., Petitdemange, S., Baker, I., Svensson, O., Burghammer, M., Mueller-Dieckmann, C., Gordon, E. J., Flot, D., McSweeney, S. M. & Leonard, G. A. (2010). *Acta Cryst.* **D66**, 855–864.
- Dickerson, J. L., McCubbin, P. T. N., Brooks-Bartlett, J. C. & Garman, E. F. (2024). *Protein Sci.* **33**, e5005.
- Garman, E. F. & Weik, M. (2023). *Curr. Opin. Struct. Biol.* **82**, 102662.
- Gonzalez, A. & Nave, C. (1994). *Acta Cryst.* **D50**, 874–877.
- Grant, T. & Grigorieff, N. (2015). *eLife*, **4**, e06980.
- Groen, J., Conesa, J. J., Valcárcel, R. & Pereiro, E. (2019). *Biophys. Rev.* **11**, 611–619.
- Groen, J., Gazi, A., Kapishnikov, S., BreLOT, A., Vos, M., Enninga, J., Pereiro, E. & Sartori-Rupp, A. (2025). *Commun. Biol.* **8**, 1677.
- Guo, J. & Larabell, C. A. (2019). *Curr. Opin. Struct. Biol.* **58**, 324–332.
- Henderson, R. (1990). *Proc. R. Soc. London B*, **241**, 6–8.
- Henderson, R. (1995). *Q. Rev. Biophys.* **28**, 171–193.
- Holler, M., Raabe, J., Wepf, R., Shahmoradian, S. H., Diaz, A., Sarafimov, B., Lachat, T., Walther, H. & Vitins, M. (2017). *Rev. Sci. Instrum.* **88**, 113701.
- Holton, J. M. (2009). *J. Synchrotron Rad.* **16**, 133–142.
- Huang, C.-Y., Meier, N., Caffrey, M., Wang, M. & Olieric, V. (2020). *J. Appl. Cryst.* **53**, 854–859.
- Karreman, M. A., Mercier, L., Schieber, N. L., Solecki, G., Allio, G., Winkler, F., Ruthensteiner, B., Goetz, J. G. & Schwab, Y. (2016). *J. Cell Sci.* **129**, 444–456.
- Kelley, K., Raczowski, A. M., Klykov, O., Jaroenlak, P., Bobe, D., Kopylov, M., Eng, E. T., Bhabha, G., Potter, C. S., Carragher, B. & Noble, A. J. (2022). *Nat. Commun.* **13**, 1857.
- Klein, S., Wachsmuth-Melm, M., Winter, S. L., Kolovou, A. & Chlanda, P. (2021). *Methods Cell Biol.* **162**, 273–302.
- Klykov, O., Bobe, D., Paraan, M., Johnston, J. D., Potter, C. S., Carragher, B., Kopylov, M. & Noble, A. J. (2022). *Bio Protoc.* **12**, e4544.
- Kuan, A. T., Phelps, J. S., Thomas, L. A., Nguyen, T. M., Han, J., Chen, C.-L., Azevedo, A. W., Tuthill, J. C., Funke, J., Cloetens, P., Pacuraneanu, A. & Lee, W. A. (2020). *Nat. Neurosci.* **23**, 1637–1643.
- Kühlbrandt, W. (2014). *Science*, **343**, 1443–1444.
- Lo, Y. H., Liao, C.-T., Zhou, J., Rana, A., Bevis, C. S., Gui, G., Enders, B., Cannon, K. M., Yu, Y.-S., Celestre, R., Nowrouzi, K., Shapiro, D., Kapteyn, H., Falcone, R., Bennett, C., Murnane, M. & Miao, J. (2019). *Sci. Adv.* **5**, eaax3009.
- Longo, E., Sancey, L., Flenner, S., Kubec, A., Bonnin, A., David, C., Müller, M. & Greving, I. (2020). *Biomed. Opt. Expr.* **11**, 5506–5517.
- Marko, M., Hsieh, C., Moberlychan, W., Mannella, C. A. & Frank, J. (2006). *J. Microsc.* **222**, 42–47.
- Nass, K. (2019). *Acta Cryst.* **D75**, 211–218.
- Naydenova, K., Peet, M. J. & Russo, C. J. (2019). *Proc. Natl Acad. Sci. USA*, **116**, 11718–11724.
- Okolo, C. A., Kounatidis, I., Groen, J., Nahas, K. L., Balint, S., Fish, T. M., Koronfel, M. A., Cortajarena, A. L., Dobbie, I. M., Pereiro, E. & Harkiolaki, M. (2021). *Nat. Protoc.* **16**, 2851–2885.
- Owen, R. L., Rudiño-Piñera, E. & Garman, E. F. (2006). *Proc. Natl Acad. Sci. USA*, **103**, 4912–4917.
- Rigort, A., Bäuerlein, F. J. B., Villa, E., Eibauer, M., Laugks, T., Baumeister, W. & Plitzko, J. M. (2012). *Proc. Natl Acad. Sci. USA*, **109**, 4449–4454.
- Rohou, A. & Grigorieff, N. (2015). *J. Struct. Biol.* **192**, 216–221.
- Saibil, H. R. (2022). *Mol. Cell*, **82**, 274–284.
- Scheres, S. H. W. (2012). *J. Mol. Biol.* **415**, 406–418.
- Shafiei, N., Stähli, D., Burger, D., Di Fabrizio, M., van den Heuvel, L., Daraspe, J., Böing, C., Shahmoradian, S. H., van de Berg, W. D. J., Genoud, C., Stahlberg, H. & Lewis, A. J. (2025). *Nat. Protoc.* **20**, 2994–3023.
- Shahmoradian, S. H., Tsai, E. H. R., Diaz, A., Guizar-Sicairos, M., Raabe, J., Spycher, L., Britschgi, M., Ruf, A., Stahlberg, H. & Holler, M. (2017). *Sci. Rep.* **7**, 6291.
- Studer, D., Graber, W., Al-Amoudi, A. & Egli, P. (2001). *J. Microsc.* **203**, 285–294.
- Teng, T. & Moffat, K. (2000). *J. Synchrotron Rad.* **7**, 313–317.
- Zheng, S. Q., Palovcak, E., Armache, J.-P., Verba, K. A., Cheng, Y. & Agard, D. A. (2017). *Nat. Methods*, **14**, 331–332.
- Zivanov, J., Nakane, T., Forsberg, B. O., Kimanius, D., Hagen, W. J., Lindahl, E. & Scheres, S. H. W. (2018). *eLife*, **7**, e42166.